Colloidal Nanocube Supercrystals Stabilized by Multipolar Coulombic Coupling

Henry Chan,[†] Arnaud Demortière,[‡,§,*] Lela Vukovic,[†] Petr Král,[†,⊥,*] and Christophe Petit[‡]

[†]Department of Chemistry, University of Illinois at Chicago, Chicago, Illinois 60607, United States , [‡]Laboratoire des Matériaux Mésoscopiques et Nanométriques, Université Pierre et Marie Curie—CNRS (UMR 7070), 4 Place Jussieu 75252 Paris Cedex 05, France, [§]Center for Nanoscale Materials, Argonne National Laboratory, 9700 S. Cass Avenue, Argonne, Illinois 60439, United States , and [⊥]Department of Physics, University of Illinois at Chicago, Chicago, Illinois 60607, United States

ABSTRACT

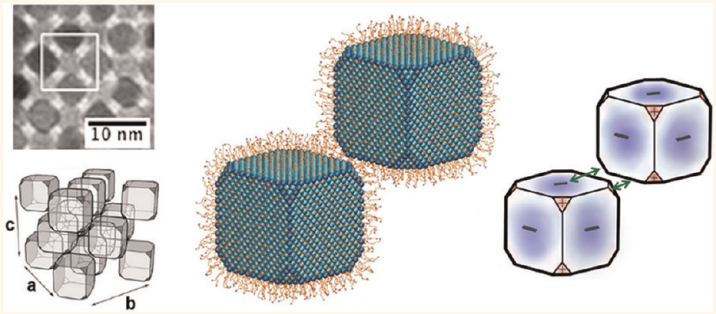

We explore microscopic principles governing the self-assembly of colloidal octylamine-coated platinum nanocubes solvated in toluene. Our experiments show that regular nanocubes with an edge length of $l_{RC} = 5.5$ nm form supercrystals with simple cubic packing, while slightly truncated nanocubes with an edge length of $l_{TC} = 4.7$ nm tend to arrange in fcc packing. We model by averaged force fields and atomistic molecular dynamics simulations the coupling forces between these nanocrystals. Our detailed analysis shows that the fcc packing, which for cubes has a lower density than simple cubic packing, is favored by the truncated nanocubes due to their Coulombic coupling by multipolar electrostatic fields, formed during charge transfer between the octylamine ligands and the Pt cores.

KEYWORDS: molecular dynamics · self-assembly · nanocubes · multipolar coupling · charge transfer

In recent years, colloidal nanoparticles (NP) of different materials,[1−4] sizes,[5] shapes,[6−16] and coatings[17−20] have been self-assembled into superlattices with many types of packing.[21−23] It is crucial to understand microscopic principles governing the processes of NP self-assembly[24] in order to control structural,[25] chemical,[26,27] and physical properties of the formed superlattices.[28,29] These novel metamaterials may exhibit new functionalities when applied in electronics,[30] optics,[31,32] magnetism,[33] and catalysis.[34,35]

In most cases, the self-assembly of colloidal NPs is thermodynamically driven by interparticle forces determined by the NP type,[36] the solvent type,[37] and other conditions used during the evaporation processes.[38−40] Typically, NPs interact with each other and the substrate[41] by van der Waals (vdW), steric, and Coulombic coupling,[42−44] originating from the NP bulk and ligands.[17,45] The related forces can be obtained in atomistic[46] or coarse-grained modeling[47] and approximated by averaged force fields acting between the NPs.[38,42,43,48−51]

Spherical colloidal NPs with isotropic interparticle coupling tend to self-assemble into close-packed fcc and hcp structures.[52] Anisotropic forces between the NPs, such as those originating in electric/magnetic dipole—dipole coupling, can lead to simple hexagonal (sh) or body-centered cubic (bcc) structures.[42,43] Nonspherical particles can have a large range of packing densities, common interfaces between crystalline facets, and intriguing geometries of void spaces, which can drastically influence the superlattice properties.[53] For example, polyhedral nanocrystals may self-organize into more open superlattices, such as cubic and octahedral nanocrystals.[10−16,54] Even though many types of superstructures have been prepared, the principles that control their self-assembly are not well understood.[16]

In this work, we combine experimental and theoretical efforts to investigate the packing principles in supercrystals formed of regular (RC) and truncated (TC) colloidal platinum nanocubes (NCs). We model with averaged force fields and atomistic molecular dynamics simulations the vdW and Coulombic coupling forces between RCs and TCs to explain their observed self-assembly in supercrystals with simple cubic (sc) and fcc packings, respectively. After careful analysis, we conclude that the looser fcc packing of TCs originates in their

* Address correspondence to ademortiere@anl.gov; pkral@uic.edu.

Received for review February 19, 2012 and accepted April 15, 2012.

Published online April 15, 2012
10.1021/nn3007338

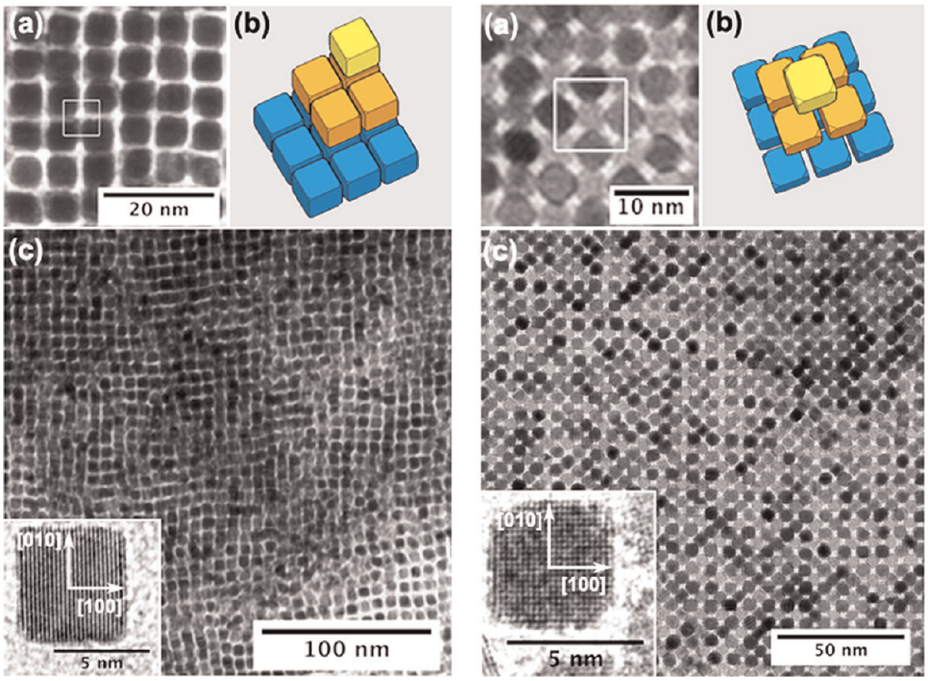

Figure 1. Experimentally observed superstructures of self-assembled regular (RCs) and truncated (TCs) colloidal octylamine-coated platinum nanocubes in toluene: (left) (a) square array of RCs; (b) scheme of the simple cubic structure; (c) multilayers of organized RCs; (inset) TEM image of a RC; (right) (a) square array of TCs; (b) scheme of the fcc structure; (c) multilayers of organized TCs; (inset) TEM image of a TC.

multipolar Coulombic coupling, where a charge is passed to the TCs from their ligands and asymmetrically redistributed in their metallic cores.

RESULTS AND DISCUSSION

Observed NC Supercrystals. We have prepared RCs and TCs coated with octylamine and solvated in toluene,[55] using a liquid−liquid phase transfer method.[13,56] The average edge lengths (between two opposite {100} faces) of the NCs are $l_{RC} = 5.5$ nm and $l_{TC} = 4.7$ nm, with a size distribution of 8% and 9%, respectively. In the insets of Figure 1c (left and right), we show HRTEM images of the {100} faces of the RC and TC, where the TC has {111} facets on its truncated corners. In our experiments, we observe that the prepared RCs form simple cubic superlattices and the TCs form fcc superlattices. The sc structures are rare in Nature, but they have been observed in Po crystals[57] and $TiO_2-P_2O_5$ NC supercrystals.[58]

In Figure 1a and c, we use TEM to show the stacking pattern of 2−4 NC layers of RC (left) and TC (right) lattices, where the white squares denote their primitive cells. The two types of superlattices are schematically shown in Figure 1b, where the RCs are positioned in the face-to-face (f−f) configuration (sc lattice) and the TCs are in the shifted corner-to-corner (c−c) configuration (fcc lattice). Sequential RC layers are stacked on top of each other (labeled as AAA), whereas each TC layer (considered along the diagonal of the fcc cube in the inset of Figure 5b) is stacked at the interstitial sites of the next layer (ABCABC), such that each successive layer is shifted by half the repetition distance. The lattice constants obtained from TEM, $a_{sc} \approx 7$ nm and $a_{fcc} \approx 11$ nm, are in good agreement with those ($A_{sc} \approx 8$ nm and $A_{fcc} \approx 11$ nm) measured by selected area electron diffraction (SAED) at 250 cm.

Recently, Yamamuro *et al*. have evaluated the vdW (ligand) coupling of model NCs in different 3D[51] and 2D stacking.[59] Their results show that the face-to-face assembly in the sc structure has the lowest potential energy. Our experiments also show that RCs form sc superlattices, but it is not clear why TCs with small corner truncations form the loose fcc superlattices. We model the NCs to understand how small changes in their shapes can lead to remarkably different superstructures.

In Figure 2a, we present SEM images of RCs forming sc supercrystals (lateral size of 0.5−2.0 μm), which are rarely formed on the substrate (inset) and often stacked in a random manner. The high-resolution SEM-FEG images in Figure 2b clearly show that a supercrystal can have a long-range order at a length scale of ~1 μm. The face of the supercrystal is a $\{100\}_{sp}$ (sp = superlattice) surface (inset Figure 2b). The magnified SEM-FEG image reveals stacking faults in the cubic arrangement, which are likely due to local inhomogeneity of NC shapes or local perturbations formed during the growth process.

Figure 3a−d shows SEM images of TCs forming fcc supercrystals. On the substrate, supercrystals with a low polydispersity and two types of morphologies are seen to form: square pyramids (Figure 3a,b) and triangular prisms (Figure 3c,d). The $[100]_{sp}$ axis of pyramidal crystals and the $[111]_{sp}$ axis of triangular crystals are normal to the substrate. From the SEM images,[13] we

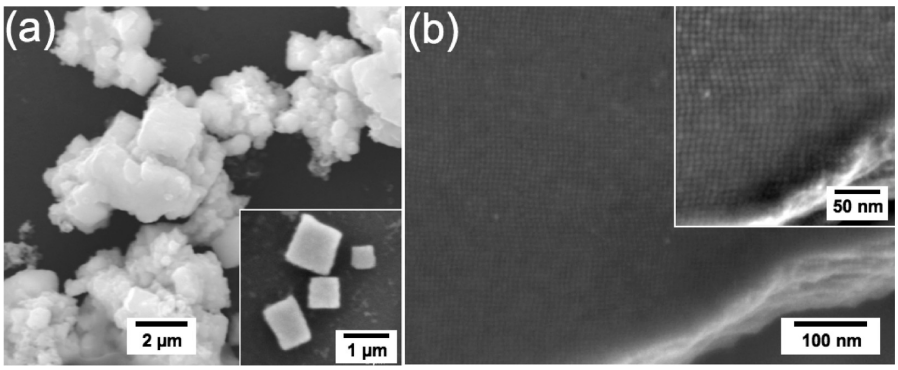

Figure 2. (a) SEM images of stacked sc supercrystals of RCs. (inset) Individual RC supercrystals. (b) SEM-FEG images of a RC supercrystal. (inset) Magnified SEM image showing the arrangement of RCs within the supercrystal.

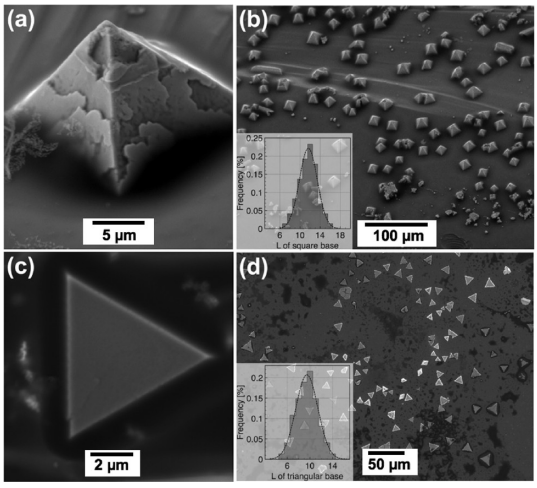

Figure 3. SEM images of fcc supercrystals of TCs. (a) Superlattice of square pyramidal shape. (b) Ensemble of square pyramidal supercrystals and their size distributions (inset). (c) Superlattice of triangular prism shape. (d) Triangular prism supercrystals and their size distribution (inset).

determined the angle between the substrate and the faces of the pyramidal crystals to be ~45°. The size of the pyramids is ~12 μm, with a size distribution of 20%, and the size of the triangles is ~9 μm, with a size distribution of 30%.

In rare cases, we observe TC supercrystals with other morphologies. In Figure 4a–c, we show SEM images of hexagonal, quasi-hexagonal, and triangular supercrystals. The multilayer textured surfaces on the faces of these supercrystals indicate that the supercrystals have similar growth processes but different growth times. In Figure 4d–f, we show SEM images of elongated, cleaved (crushed) with a well-defined internal structure, and decahedron supercrystals; the 5-fold symmetry could be due to multiple twinning.[60] These supercrystals are likely formed due to the presence of faults in the fcc stacking or the emergence of other growth axes induced by particle–substrate interactions.

Supercrystal Growth. In order to prepare uniform supercrystals with a long-range order, shown in Figures 2–4, slow crystallization conditions must be guaranteed. We use a glass tube to create a limited air/solution interface, which allows us to achieve a very slow evaporation rate (8 days) of toluene (bp = 110 °C) at 25 °C. Our TEM specimens are prepared by immersing a carbon-coated TEM grid in the glass tube containing 200 μL of colloidal solution with a concentration of 2×10^{-5} mol/L. SEM specimens are obtained by immersing a silicon substrate (Si wafer) in the glass tube containing 2 mL of the same colloidal solution. It is useful to describe the nucleation and growth of NC crystals in more detail to disclose potential principles of their self-assembly.

Supercrystal Nucleation. The growth of supercrystals of colloidal NCs starts by the spontaneous formation of a crystalline nucleus, which takes part either homogeneously in the solution or heterogeneously on a substrate.[61] The energy barrier of homogeneous nucleation, ΔG_N^{homo}, is usually larger (more limiting) than the barrier of heterogeneous nucleation, ΔG_N^{hete}. The barriers can be affected by the strength of interparticle interactions, the solvent evaporation rate, NC–substrate interfacial properties, and other factors.

In RCs, the strong vdW interactions between their {100} faces may allow the sc superlattice to form in solution. Once formed, the crystallites attach to the substrate, where they continue to grow, as seen in Figure 2a. Their nucleation appears to be mainly homogeneous, since the supercrystals are in random positions on the substrate. Consequently, diffraction patterns reveal only homogeneous rings, and the small-angle X-ray diffraction (SA-XRD) pattern indicates the absence of a single-growth axis.[13]

On the other hand, the fcc superlattice aggregates seem to be stabilized by corner-to-corner interactions of the TCs, which might be difficult to materialize in a repetitive manner without a substrate. In Figure 3, we seem to observe that NCs self-organize on substrates, where they grow into supercrystals with different morphologies, depending on the facets lying on the substrate. The initial square arrangement of the $\{100\}_{sp}$ basic plane yields a pyramidal fcc crystal, whereas a hexagonal layer, $\{111\}_{sp}$ basic plane, yields a triangular fcc crystal (no C_3 symmetry due to NCs in

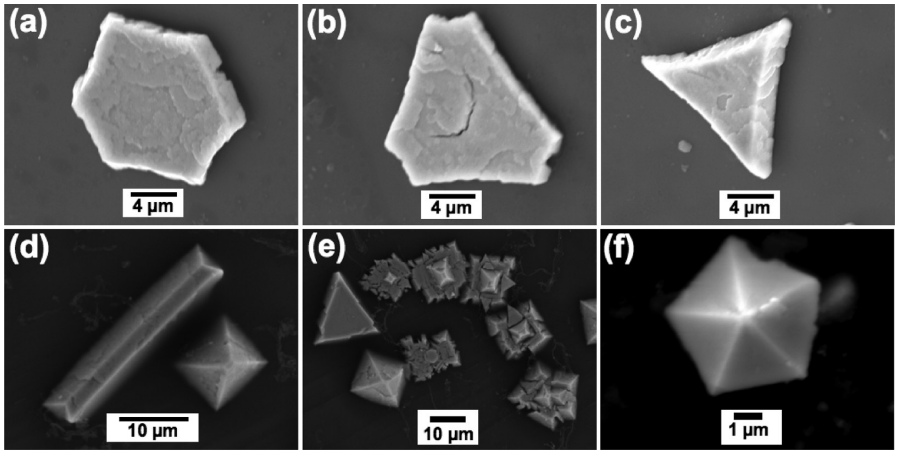

Figure 4. SEM images of TC supercrystals. (a) Hexagonal shape. (b) Quasi-hexagonal. (c) Triangular. (d) Elongated. (e) Cleaved (crushed). (f) Decahedral.

the lattice points). This is confirmed by previous SA-XRD observations, which reveal the $[001]_{sp}$ growth axis (perpendicular to the substrate) for the pyramidal supercrystals and the $[111]_{sp}$ growth axis for the triangular supercrystals.[13]

Deliberation of the NC Coupling Forces. In order to understand what drives the self-assembly in the observed RCs and TCs superstructures, we will try to characterize the dominant forces between the NCs. Although the observed superlattices are probably nucleated in the colloidal phase (solution or substrate), they can be further stabilized during the solvent evaporation. We can estimate these processes from the NC-binding Gibbs free energy, $\Delta G = \Delta H - T\Delta S$, in *solvent* and *vacuum*. We briefly discuss the important terms involved in ΔG.

In principle, large polarizabilities of the metal NC cores result in dispersion forces that can induce the self-assembly of colloidal NPs at room temperature.[38,49] The strength of this bulk vdW core−core coupling, ΔH^{vdW}_{core}, grows with the polarizabilities of the interacting NPs. The Pt NC cores are much more polarizable than the toluene solvent and the octylamine ligands on the NCs, so the strength of vdW coupling (per unit volume) ranks as core−core > core−ligand > ligand−ligand ≈ ligand−solvent. When the solvent and ligands are chemically similar, we can neglect the ligand−ligand vdW coupling and consider just the core−core vdW coupling.[42,43] We suspect that this coupling alone cannot explain the self-assembly of loose fcc superstructures formed by the TCs. It is also unlikely that the vdW coupling associated with the ligands (of different densities[25]) close to the (shifted) corners of neighboring TCs could create the local minima in ΔG, which is necessary for the fcc lattice stabilization.

The loose fcc superstructures might be self-assembled by *directional forces* acting between colloidal TCs and providing the local energy minima in ΔG around their corners. Such local minima could originate from a multipolar Coulombic coupling, caused for example by partial charge transfer between the ligands and the Pt NC cores.[62] Electrons in the vicinity of the ligand binding sites (Pt atoms) can be transferred to the more electronegative octylamine ligands (N atoms). Inside the metallic NC, the charge can freely redistribute and locally charge the NC, as schematically shown in Figure 6a. The (neutral) TCs can interact with each other in toluene at relatively large distances, as characterized by ΔH^{eleo}_{NC}, and direct the self-assembly of fcc superlattices.

Once the solvent is evaporated (vacuum), the ligand−ligand vdW coupling enthalpy, ΔH^{vdW}_{ligand}, and the related entropy, ΔS_{ligand}, can dominate in ΔG. When the ligands interdigitate more, their entropy, ΔS_{ligand}, decreases (limited space and ligand conformations), which counterbalances the growth of ΔH^{vdW}_{ligand}. The ligand−ligand coupling might seal the superstructure prestabilized in solvent by the Coulombic coupling and the bulk vdW core−core coupling.

Modeling of the NC Self-Assembly. In the following, we will calculate the various contributions to ΔG to estimate which of them might activate and guide the NC self-assembly. First, we model the microscopic bulk vdW core−core coupling between NCs by average force fields. Then, we evaluate by atomistic molecular dynamics (MD) simulations the NC coupling associated with their polarized ligands and NC cores.

A. Microscopic Modeling (Bulk vdW Coupling). The (NC−core) vdW potential energy between two NCs (*i*th and *j*th) can be approximated by the Hamaker pairwise summation,[43,63]

$$V = V^{vdW}_{core}(ij) = -\frac{A}{\pi^2}\int_{V_i}\int_{V_j}\frac{1}{r_{ij}^6}d\vec{r}_i\, d\vec{r}_j \qquad (1)$$

where A is the Hamaker constant that depends on the type of NC core and r_{ij} is the distance between atoms (microscopic elements) of the two NCs.

Due to the fast decay of the vdW coupling (the $1/r^6$ term), we consider interactions only between the NC

and its first neighbors. We obtain the vdW potential energy per NC in the sc superlattice,

$$V^{sc} = \frac{1}{2}(6V_{f-f} + 12V_{e-e} + 8V_{dc-dc}) \quad (2)$$

where the subscripts in V indicate the face-to-face (f−f), edge-to-edge (e−e), and direct corner-to-corner (dc−dc) NC coupling terms (in the last term, NC corners are frontally arranged with respect to each other). Likewise, we obtain the vdW energy for the fcc superlattice,

$$V^{fcc} = \frac{1}{2}(4V_{f-f} + 4V_{e-e} + 8V_{c-c}) \quad (3)$$

where we consider the intralayer face-to-face (f−f), intralayer edge-to-edge (e−e), and interlayer shifted corner-to-corner (c−c) NC coupling terms (we mean horizontal layers shown in the inset of Figure 5b); dc−dc is replaced by c−c because the corner facets of the TCs in the fcc superlattice are not aligned. In the calculations, we use the averaged experimental edge lengths (between two opposite {100} faces) of $l_{RC} = 5.5$ nm and $l_{TC} = 4.7$ nm. The {111} corner facets of the TC are characterized by the experimental length of the corner truncation, $\alpha = 0.85$ nm, measured along the NC edge.

First, we calculate V^{sc} for RCs and TCs by varying the face-to-face internanocube distance, d_{sc}, as shown in Figure 5a. The Hamaker constant for Pt−Pt coupling (through octylamine ligands) is approximated by its value for gold−gold coupling (through dodecanethiol), $A \approx 2$ eV.[64] The results show that V^{sc} is always smaller (more stable) for RCs than for TCs. The vertical line depicted in Figure 5a marks the experimentally observed interparticle distance of RCs in the sc superlattice. At this distance, determined by the ligand length, we find that $V^{sc}_{RC} = -13.1$ kcal/mol and $V^{sc}_{TC} = -7.5$ kcal/mol. The difference is caused by different sizes of the NCs and the presence of small truncations in TCs.

Next, we calculate V^{fcc} for RCs and TCs, by varying their intralayer (a_{fcc}, b_{fcc}) and interlayer (c_{fcc}) distances. Since the fcc superlattice formed of TCs has C_4 symmetry (seen in Figure 1b (right)), we consider that $a_{fcc} = b_{fcc}$. The NCs in the fcc superlattice have larger intralayer distances than those in the sc superlattice, but their interlayer distances are smaller due to the ABCABC stacking pattern. In Figure 5b, we show the V^{fcc} energy contour map calculated for the TCs. The potential energy of $V^{fcc}_{TC} = -6.7$ kcal/mol is obtained at the point $a_{fcc} = b_{fcc} = c_{fcc} = 11$ nm. This point marks the experimentally observed shifted corner-to-corner TC configuration, where neighboring TCs have a subnanometer (interlayer) face-to-face distance of $d_{fcc} = 0.8$ nm (based on $c_{fcc} = 11$ nm and $l_{TC} = 4.7$ nm). In Figure 5b, we also show that neighboring TCs in the fcc structure do not have aligned corners. The sloped line at the bottom of the contour map marks the configurations where the corner facets of the TCs are aligned ($a_{fcc} = b_{fcc} = \sqrt{2}c_{fcc}$).

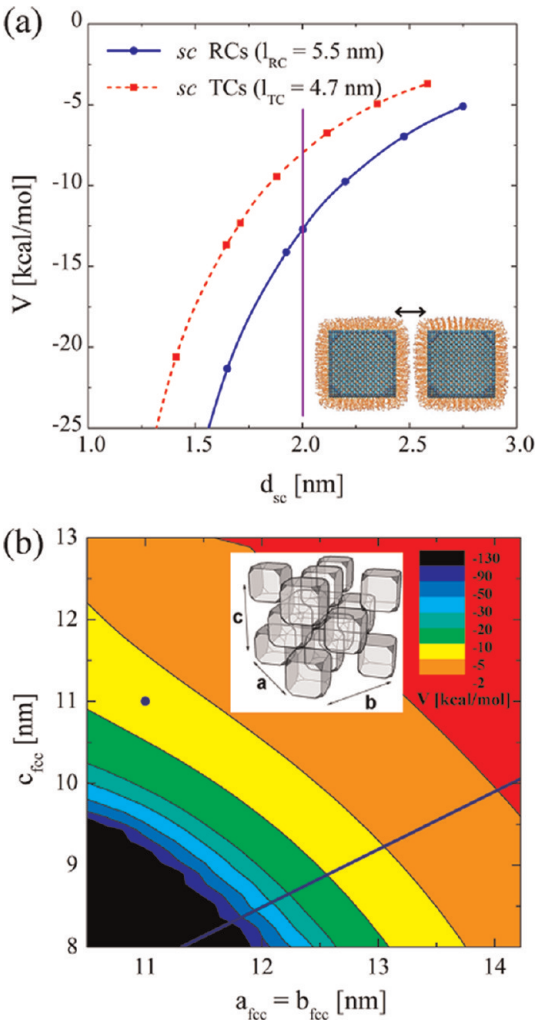

Figure 5. (a) vdW potential energy per particle for sc structures, V^{sc}, of RCs and TCs with respect to the face-to-face internanocube distance, d_{sc}. The vertical line marks the experimentally observed d_{sc} for RCs in the sc superlattice. (b) vdW potential energy per particle for fcc structures, V^{fcc}, of TCs with respect to the parameters $a_{fcc} = b_{fcc}$ and c_{fcc}. The line ($a_{fcc} = b_{fcc} = \sqrt{2}c_{fcc}$) represents parameters for which the TCs have aligned corner facets.

The energy contour map shows that the large intralayer distance between TCs in the fcc superlattice (a_{fcc}, b_{fcc}) could be stabilized by the small interlayer distance (included in c_{fcc}). The fact that TCs experimentally assemble with a small (interlayer) face-to-face distance ($d_{fcc} = 0.8$ nm) might indicate that the ligand density is lower (less steric repulsion) on the {111} corner facets than on the {100} faces. However, it is difficult to argue why TCs in the experiment do not align their corner facets, which should give a stronger corner-to-corner coupling. The bulk vdW coupling also does not give a clear "visible" local minimum at large NC separations, which is necessary for the formation of the fcc structure.

B. Atomistic Modeling. The above mean-field model shows that bulk vdW forces might allow TCs to self-assemble into loose fcc structure, but the results do not

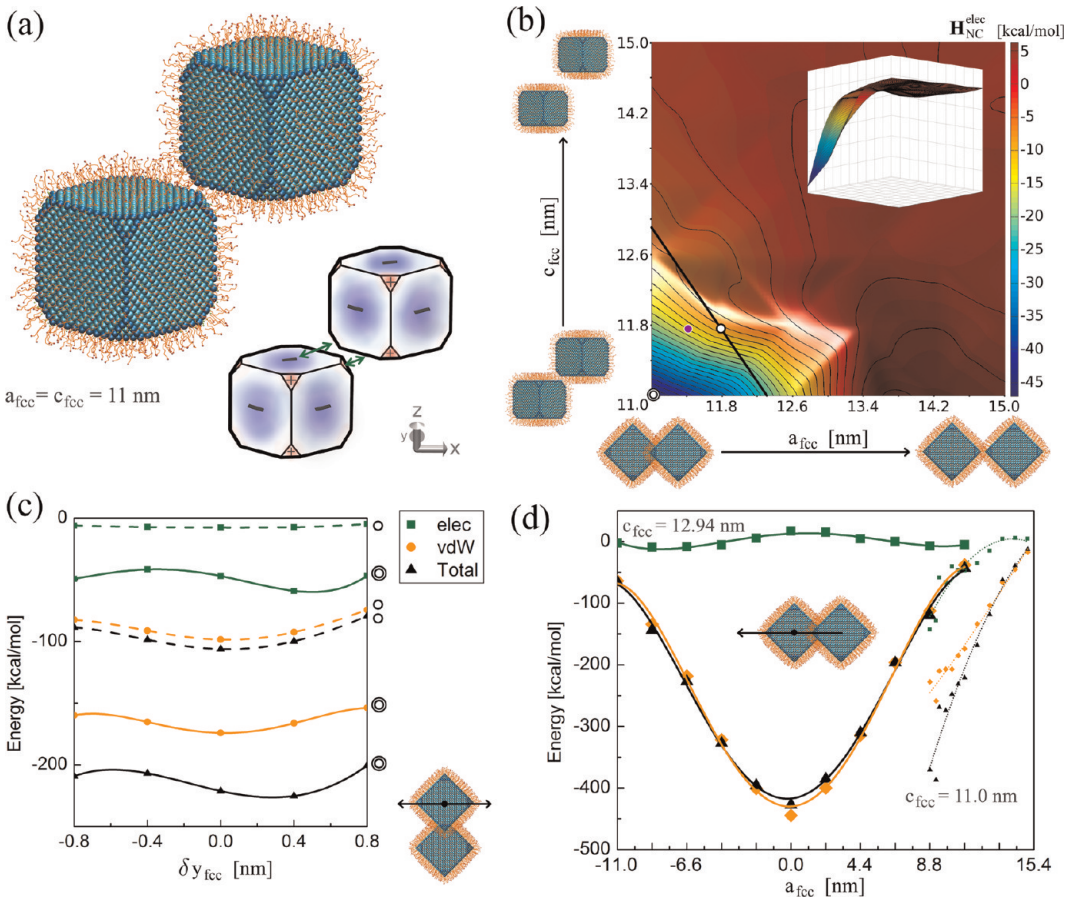

Figure 6. (a) Atomistic model of TCs in the experimentally predicted c−c configuration, with H atoms hidden. The schematic drawing shows one possible charge distribution on the surface of the TCs that can stabilize the structure through the attractions shown by the arrows. (b) Contour plot of the Coulombic coupling energy of TCs starting from the predicted c−c configuration. The inset shows a 3D view of the energy surface. (c) Coulombic and vdW (ligand) coupling energies of TCs that are slightly shifted from the $a_{fcc} = c_{fcc} = 11.0$ nm and $a_{fcc} = c_{fcc} = 11.8$ nm configurations along the *y*-direction. The two configurations are labeled by a single-ring or double-ring icon on the right of each curve. (d) The Coulombic and vdW (ligand) coupling energies of NCs as a function of a_{fcc} are evaluated to cover the transition from the c−c configuration to the f−f configuration at the height of $c_{fcc} = 12.94$ nm and $c_{fcc} = 11.0$ nm.

explain the observed shift of corners, and they do not provide a significant local energy minimum that would prevent the loose fcc structure from switching to the more compact sc structure. To address these issues, we use atomistic molecular dynamics simulations to model molecular forces between neighboring TCs. We assume that TCs interact through vdW coupling of their octylamine ligands and Coulombic coupling between partial charges on their ligands and cores, formed due to the charge transfer along N−Pt bonds.

Model of the NCs. In Figure 6a we show our atomistic model of two TCs in the shifted corner-to-corner (c−c) configuration. Each TC has a Pt core protected by a monolayer of octylamine ligands, with the edge length (between two opposite {100} faces) of l_{TC} = 4.704 nm, based on the experimental value of l_{TC} = 4.7 nm. The {111} corner facets are characterized by the corner truncation parameter of α = 0.784 nm, obtained by removing three Pt layers; it is close to the experimental value of α = 0.85 nm.

In the MD simulations, we maintain the shape and rigidity of the core by Pt−Pt bonds with a large bond strength of $\sim 10^4$ kcal/mol Å^2, added in the force field. The NC core has fcc packing with the lattice constant of a = 3.92 Å, derived from the equilibrium Pt−Pt bond length of b_0 = 2.77 Å. Each TC core has 7758 Pt atoms, where 1494 and 24 of them are exposed on the TC {100} faces and {111} facets, respectively, excluding the 180 Pt atoms that are on the edges.

Next, we attach octylamine ligands to the surface of the Pt core. The ligand densities and distributions cannot be observed from our TEM measurements, due to the low elemental contrast of molecular ligands. We estimate their local densities by assuming that ligands preferably bind to less coordinated Pt atoms. The coordination numbers for Pt atoms on the {100} faces, edges between two {100} faces, {111} facets, and edges around the {111} facets are 8, 5, 9, and 7, respectively, whereas bulk Pt atoms have a coordination number of 12. In our model, we attach 1 ligand onto each Pt atom on the edges and distribute ligands

randomly and evenly on the faces with the density of 2 per 5 Pt atoms. We do not attach ligands on the small corner facets (3 Pt atoms per facet) due to the high steric hindrance between those ligands and ligands that are already attached to the edges. Even though these distributions are rather heuristic, their exact form does not seem to influence much the stability of the self-assembled TCs (see later).

Atomic charges on the (neutral) ligands are based on the CHARMM32 force field.[65] We model the Pt−N charge transfer by adding −0.4 e to the Pt-bound N atoms of the ligands and 0.4 e to the ligand-hosting Pt atoms. The magnitude of the charge transfer is closely related to the results obtained from *ab initio* studies of NH_x species absorbed on Pt surfaces.[62] We keep the rest of the Pt atoms neutral and do not consider the (slight) charge redistribution on the metallic Pt core. If the positive charges on the Pt atoms are left to freely redistribute inside the metallic TC, they would cancel the field in its interior. Their repulsion would cause a slight shift from the area under the ligands toward the corners and lead to the surface charge densities schematically shown in Figure 6a. In our MD simulations, the presence of fixed Pt−N dipoles on the TC faces generates an electric field with the same multipolar symmetry but a smaller strength. When the TCs self-assemble in the fcc packing in the experimental system, their charge distribution might be further modified due to the rearrangement (detachment and reattachment) of ligands. Therefore, it is likely that the self-assembled structures have some tolerance with respect to the exact distribution of ligands and the core charging.

Modeling of the NC Coupling. We will simulate these RCs and TCs as described in the Methods section. First, we search for additional local minima in ΔG that can help to stabilize the self-assembled superstructures. As discussed above, the vdW ligand−ligand coupling should be relatively small in solvent (toluene), which is similar to the ligands. Therefore, the additional minima can potentially originate from the Coulombic coupling between the NCs.

During the MD simulations, we keep two adjacent NCs aligned and shifted with respect to each other in a vacuum (to simulate a smaller number of atoms) and evaluate their corner-to-corner coupling. We mainly focus on their Coulombic coupling, which is not much affected by the lack of nonpolar solvent, while the vdW coupling is much stronger in its absence. The NCs are placed in a large cubic unit cell (20 nm in length), with periodic boundary conditions applied (NVT ensemble). This (simulation) unit cell is oriented the same way as the unit cells in the sc and fcc lattices (see Figure 1), so that a_{fcc}, b_{fcc}, and c_{fcc} are distances along the simulation *x*, *y*, and *z* axes, respectively. The centers of two adjacent NCs in the sc lattice are separated by the distance d_{NC-NC}, whereas those in the fcc lattice (interlayer) are separated in the *x*, *y*, and *z* directions by about one-half of the lattice parameters a_{fcc}, b_{fcc}, and c_{fcc}, respectively. In the simulations, we vary some of these parameters (while fixing others) to evaluate the NC-binding energy.

In each simulation, we allow the ligands to relax while the NC-core atoms are spatially fixed. We first minimize the system energy for ∼1 ns and then equilibrate the system for ∼2 ns at the temperature T = 300 K. We use the last 1.5 ns of the simulation trajectories to evaluate the average Coulombic and vdW (ligand) coupling energy. When we optimize the binding position of the NCs, we briefly release the core atoms and run longer simulations to allow NC movements. We evaluate nonbonded (Coulombic and vdW) interactions of the TCs by pairwise summations of the coupling energies between atoms of both NCs.

TC Binding Energies. We first calculate the Coulombic and vdW (ligand) binding energies between two adjacent TCs in the shifted corner-to-corner (c−c) and face-to-face (f−f) configurations. In Figure 6b, we present the total Coulombic energy for TCs in the c−c configurations. We plot the potential energy surface as a function of the a_{fcc} and c_{fcc} parameters (b_{fcc} is not defined here), starting from the experimentally observed TC separation of $a_{fcc} = c_{fcc}$ = 11.0 nm. A 3D view of the energy surface is shown in the inset. In the studied range of the lattice parameters, the lowest value of the electrostatic energy, $E_{elec} \approx -47.0$ kcal/mol, is obtained at the experimental TC separation, $a_{fcc} = c_{fcc}$ = 11.0 nm. If we remove the charges associated with the charge separation along the Pt−N bonds (ligand−NC), we get $E_{elec} \approx 12.9$ kcal/mol for the same TC separation. These coupling energies are significantly larger than those found above for the bulk vdW coupling. Moreover, only the coupling between two NC neighbors is (so far) included in the energy.

If we allow the ligated TCs to spontaneously stabilize their positions, we find that they go to the point of a_{fcc} = 11.4 nm, c_{fcc} = 11.8 nm (see point in Figure 6b), rather than to the experimental point of $a_{fcc} = c_{fcc}$ = 11.0 nm. This is likely caused by the fact that in the experiment the ligands can migrate on the NC surfaces and be further redistributed upon the lattice formation to minimize the coupling energy.[66] The simulations of these relaxed TCs are only done for 2−3 ns to prevent their rotation. In this stabilization, both enthalpic and entropic contributions are involved in ΔG.

To estimate the local stability of the TCs with shifted corners, we calculate the binding energy as their truncated corners "slide" on each other. In Figure 6b, this motion goes along the straight line with a slope of $-\sqrt{2}$, which passes through the chosen point of $a_{fcc} = c_{fcc}$ = 11.8 nm. We evaluate E_{elec} along this line up to the point where the center of the two TC facets is at the closest distance and aligned (a_{fcc} = 13.8 nm, c_{fcc} = 9.0 nm). The lowest Coulombic energy along this line is $E_{elec} \approx -21.4$ kcal/mol, which is found at the point a_{fcc} = 12.6 nm and c_{fcc} = 10.7 nm. This gives a small

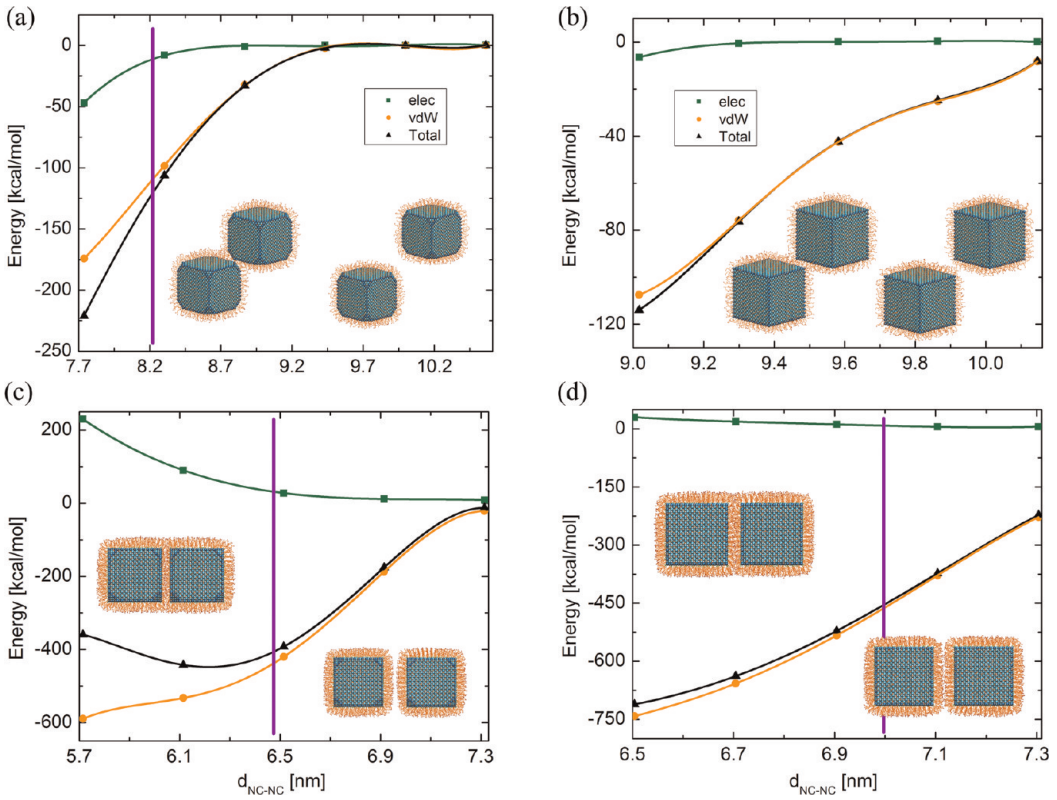

Figure 7. Coulombic and vdW (ligand) coupling energies of NCs as a function of the (interlayer) center-to-center internanocube distance, d_{NC-NC}, for (a) TCs in the c−c configuration; (b) RCs in the c−c configuration; (c) TCs in the f−f configuration; (d) RCs in the f−f configuration. Schematic drawings in each plot show the configurations of the two end points. The vertical lines show the equilibrated distances of NCs with relaxed cores.

energy barrier of $\Delta E_{elec} \approx 1.6$ kcal/mol, which keeps the TC corners shifted. If we consider a free redistribution of the charges in the TCs, the energy barrier will likely be higher.

In Figure 6c, we show the dependence of the total Coulombic and vdW energies in the TC pair, as we shift one TC with respect to the other along the *y*-direction. We define δy_{fcc} as the shift from the symmetric position. We choose two *x* and *z* positions of the TCs, $a_{fcc} = c_{fcc} = 11.0$ nm (double ring in Figure 6b,c) and $a_{fcc} = c_{fcc} = 11.8$ nm (single ring in Figure 6b,c). As discussed earlier, the vdW energy mostly contributes to the NC stabilization after the removal of solvent (its value is then large, as seen here). We can see that for the experimental distances the vdW energy has a minimum at $\delta y_{fcc} = 0$, while the Coulombic energy minimum is shifted to $\delta y_{fcc} = 0.6$ nm. This slight asymmetry is caused by the random distribution of ligands on the TCs. At the larger separation (11.8 nm), the energy minima are already at $\delta y_{fcc} = 0$.

Upon the removal of the solvent, the vdW energy of the coupled ligands becomes large in the f−f configuration. The question is if the TCs stay in c−c configuration or spontaneously switch to the f−f configuration. In order to do so, the TCs would need to be lifted from the potential energy minimum at $c_{fcc} = 11.8$ nm (equilibrium distance of the c−c configuration) to the elevation of $c_{fcc} = 12.94$ nm (equilibrium distance of the f−f configuration), to be above the steric (ligand) barrier. This lifting is associated with a Coulombic barrier of ~14 kcal/mol, which is not thermally accessible. The barrier is about 3 times larger if done from the experimentally observed height of $c_{fcc} = 11.0$ nm. In Figure 6d, we fix the TC height to $c_{fcc} = 12.94$ nm and show the Coulombic and vdW energies as the TCs slide on their faces. The variation of the Coulombic energy is very small, but the vdW energy has a deep minimum at $a_{fcc} = 0$ nm (f−f configuration). We also show by dashed line the partial dependence of these energies calculated for the experimental TC height of $c_{fcc} = 11$ nm (ligand repulsion prevents completion).

Comparison of the TC and RC Binding Energies. In Figure 7, we compare the Coulombic and vdW (ligand) coupling energies of TCs (left) and RCs (right) in the c−c (top) and f−f (bottom) configurations. These energies are calculated as a function of the center-to-center distance of two (nearest) NCs with fixed cores, where $a_{fcc} = c_{fcc}$ and $\delta y_{fcc} = 0$. First, we consider the c−c configurations (Figure 6a,b). If we align both the RCs and TCs in a similar way, d_{NC-NC} in TCs is ~1 nm smaller than in RCs, due to the smaller sizes of their cores ($l_{TC} = 4.7$ nm and $l_{RC} = 5.1$ nm). If the NC cores are free to move, the (relaxed) TCs tend to stabilize in the c−c configuration (the dark point in Figure 6b at

a_{fcc} = 11.4 nm and c_{fcc} = 11.8 nm), shown by the vertical line in Figure 7a, while RCs continue to slide to the f−f configuration. In the c−c configuration the Coulombic coupling energy (relevant in solution) is negative and larger for TCs, while in the f−f configurations it is positive and larger for TCs (Figure 6c,d). Both NCs in a vacuum can stabilize in the f−f configuration; their equilibrium d_{NC-NC} are shown by the vertical lines in Figure 6c,d.

If we compare the vdW (ligand) energies in a vacuum for both configurations, we can see that the f−f configuration is globally more stable for both RCs and TCs. In the solvent, the vdW coupling should be small, and the ligands might even cause repulsion between the NPs.[67] Therefore, it is the Coulombic coupling (together with the bulk vdW coupling) that can guide and stabilize the loose fcc structure of TCs.

CONCLUSIONS

In summary, we have prepared sc and fcc superlattices of ligated regular and truncated Pt nanocubes, respectively, and used microscopic and atomistic modeling to explain the remarkably different observed structures. Our results indicate that the fcc packing can be stabilized by Coulombic coupling between multipolar electrostatic fields of charged TCs, which originate from the charge transfer between their ligands and platinum cores. This coupling creates a local energy minimum when the TCs have adjacent (shifted) corners, which can retain the fcc packing in solvent and vacuum against global stabilization of the sc structure. These results could be used in guiding the experimental preparation of novel supercrystals with many potential applications.

METHODS

We simulate the pairs of RCs and TCs by atomistic molecular dynamics simulations, using NAMD[68,69] and the CHARMM32 force field.[65] During our simulations, we keep the temperature fixed by the Langevin dynamics with the damping constant of γ_{Lang} = 1 ps^{-1}. The nonbonded interaction switching distance is set to 8 Å, and the cutoff is set to 10 Å. The systems are simulated as NVT ensembles, where the particle mesh Ewald summation[70] is considered for the Coulombic coupling.

Conflict of Interest: The authors declare no competing financial interest.

Acknowledgment. The authors would like to express their gratitude to Cédric Leuvrey, IPCMS, UMR 7504 CNRS/UdS, Strasbourg, France, for his assistance with the characterization of supercrystals using SEM-FEG, and Pascale Launois and Pierre-Antoine Albouy, LPS, UMR 8502 CNRS/Université Paris Sud, Orsay, France, for their valuable discussions. L.V. acknowledges support from the UIC Dean Scholar Award. The presented calculations have been partly realized on the NERSC and NCSA supercomputer networks.

REFERENCES AND NOTES

1. Murray, C. B.; Sun, S.; Doyle, H.; Betley, T. Monodisperse 3d Transition-Metal (Co, Ni, Fe) Nanoparticles and Their Assembly into Nanoparticle Superlattices. *Mater. Res. Soc. Bull.* **2001**, *26*, 985–991.
2. Alivisatos, A. P. Semiconductor Clusters, Nanocrystals, and Quantum Dots. *Science* **1996**, *271*, 933–937.
3. Buck, M. R.; Bondi, J. F.; Schaak, R. E. A Total-synthesis Framework for the Construction of High-Order Colloidal Hybrid Nanoparticles. *Nat. Chem.* **2012**, *4*, 37–44.
4. Dong, A.; Ye, X.; Chen, J.; Murray, C. B. Two-Dimensional Binary and Ternary Nanocrystal Superlattices: The Case of Monolayers and Bilayers. *Nano Lett.* **2011**, *11*, 1804–1809.
5. Chang, C.-C.; Wu, H.-L.; Kuo, C.-H.; Huang, M. H. Hydrothermal Synthesis of Monodispersed Octahedral Gold Nanocrystals with Five Different Size Ranges and Their Self-Assembled Structures. *Chem. Mater.* **2008**, *20*, 7570–7574.
6. Manna, L.; Scher, E. C.; Alivisatos, A. P. Synthesis of Soluble and Processable Rod-, Arrow-, Teardrop-, and Tetrapod-Shaped CdSe Nanocrystals. *J. Am. Chem. Soc.* **2000**, *122*, 12700–12706.
7. Peng, X.; Manna, L.; Yang, W.; Wickham, J.; Scher, E.; Kadavanich, A.; Alivisatos, A. P. Shape Control of CdSe Nanocrystals. *Nature* **2000**, *404*, 59–61.
8. Puntes, V. F.; Zanchet, D.; Erdonmez, C. K.; Alivisatos, A. P. Synthesis of hcp-Co Nanodisks. *J. Am. Chem. Soc.* **2002**, *124*, 12874–12880.
9. Jun, Y.-W.; Casula, M. F.; Sim, J.-H.; Kim, S. Y.; Cheon, J.; Alivisatos, A. P. Surfactant-Assisted Elimination of a High Energy Facet as a Means of Controlling the Shapes of TiO_2 Nanocrystals. *J. Am. Chem. Soc.* **2003**, *125*, 15981–15985.
10. Wang, Z. L. Transmission Electron Microscopy of Shape-Controlled Nanocrystals and Their Assemblies. *J. Phys. Chem. B* **2000**, *104*, 1153–1175.
11. Tao, A. R.; Ceperley, D. P.; Sinsermsuksakul, P.; Neureuther, A. R.; Yang, P. Self-Organized Silver Nanoparticles for Three-Dimensional Plasmonic Crystals. *Nano Lett.* **2008**, *8*, 4033–4038.
12. Glotzer, S. C.; Solomon, M. J. Anisotropy of Building Blocks and Their Assembly into Complex Structures. *Nat. Mater.* **2007**, *6*, 557–562.
13. Demortière, A.; Launois, P.; Goubet, N.; Albouy, P.-A.; Petit, C. Shape-Controlled Platinum Nanocubes and Their Assembly into Two-Dimensional and Three-Dimensional Superlattices. *J. Phys. Chem. B* **2008**, *112*, 14583–14592.
14. Lu, W.; Liu, Q.; Sun, Z.; He, J.; Ezeolu, C.; Fang, J. Super Crystal Structures of Octahedral c-In_2O_3 Nanocrystals. *J. Am. Chem. Soc.* **2008**, *130*, 6983–6991.
15. Zheng, R. K.; Gu, H.; Xu, B.; Fung, K. K.; Zhang, X. X.; Ringer, S. P. Self-Assembly and Self-Orientation of Truncated Octahedral Magnetite Nanocrystals. *Adv. Mater.* **2006**, *18*, 2418–2421.
16. Quan, Z.; Fang, J. Superlattices with Non-Spherical Building Blocks. *Nano Today* **2010**, *5*, 390–411.
17. Murray, C. B.; Kagan, C. R.; Bawendi, M. G. Self-Organization of CdSe Nanocrystallites into Three-Dimensional Quantum Dot Superlattices. *Science* **1995**, *270*, 1335–1338.
18. Kovalenko, M. V.; Scheele, M.; Talapin, D. V. Colloidal Nanocrystals with Molecular Metal Chalcogenide Surface Ligands. *Science* **2009**, *324*, 1417–1420.
19. Martin, J. E.; Wilcoxon, J. P.; Odinek, J.; Provencio, P. Control of the Interparticle Spacing in Gold Nanoparticle Superlattices. *J. Phys. Chem. B* **2000**, *104*, 9475–9486.
20. Demortière, A.; Buathong, S.; Pichon, B. P.; Panissod, P.; Guillon, D.; Bégin-Colin, S.; Donnio, B. Nematic-like Organization of Magnetic Mesogen-Hybridized Nanoparticles. *Small* **2010**, *6*, 1341–1346.
21. Murray, C. B.; Kagan, C. R.; Bawendi, M. G. Synthesis and Characterization of Monodisperse Nanocrystals and

Close-Packed Nanocrystal Assemblies. *Annu. Rev. Mater. Sci.* **2000**, *30*, 545–610.
22. Puntes, V. F.; Krishnan, K. M.; Alivisatos, A. P. Colloidal Nanocrystal Shape and Size Control: The Case of Cobalt. *Science* **2001**, *291*, 2115–2117.
23. Burda, C.; Chen, X.; Narayanan, R.; El-Sayed, M. A. Chemistry and Properties of Nanocrystals of Different Shapes. *Chem. Rev.* **2005**, *105*, 1025–1102.
24. Motte, L.; Billoudet, F.; Pileni, M. P. Self-Assembled Monolayer of Nanosized Particles Differing by Their Sizes. *J. Phys. Chem.* **1995**, *99*, 16425–16429.
25. Choi, J. J.; Bealing, C. R.; Bian, K.; Hughes, K. J.; Zhang, W.; Smilgies, D.-M.; Hennig, R. G.; Engstrom, J. R.; Hanrath, T. Controlling Nanocrystal Superlattice Symmetry and Shape-Anisotropic Interactions through Variable Ligand Surface Coverage. *J. Am. Chem. Soc.* **2011**, *133*, 3131–3138.
26. Park, J.; Kang, E.; Son, S.; Park, H.; Lee, M.; Kim, J.; Kim, K.; Noh, H.-J.; Park, J.-H.; Bae, C.; *et al*. Monodisperse Nanoparticles of Ni and NiO: Synthesis, Characterization, Self-assembled Superlattices, and Catalytic Applications in the Suzuki Coupling Reaction. *Adv. Mater.* **2005**, *17*, 429–434.
27. Bell, A. T. The Impact of Nanoscience on Heterogeneous Catalysis. *Science* **2003**, *299*, 1688–1691.
28. Mueggenburg, K. E.; Lin, X.-M.; Goldsmith, R. H.; Jaeger, H. M. Elastic Membranes of Close-packed Nanoparticle Arrays. *Nat. Mater.* **2007**, *6*, 656–660.
29. Chen, C.-F.; Tzeng, S.-D.; Chen, H.-Y.; Lin, K.-J.; Gwo, S. Tunable Plasmonic Response from Alkanethiolate-Stabilized Gold Nanoparticle Superlattices: Evidence of Near-Field Coupling. *J. Am. Chem. Soc.* **2007**, *130*, 824–826.
30. Andres, R. P.; Bielefeld, J. D.; Henderson, J. I.; Janes, D. B.; Kolagunta, V. R.; Kubiak, C. P.; Mahoney, W. J.; Osifchin, R. G. Self-Assembly of a Two-Dimensional Superlattice of Molecularly Linked Metal Clusters. *Science* **1996**, *273*, 1690–1693.
31. Zaitseva, N.; Dai, Z. R.; Leon, F. R.; Krol, D. Optical Properties of CdSe Superlattices. *J. Am. Chem. Soc.* **2005**, *127*, 10221–10226.
32. Grzelczak, M.; Mezzasalma, S. A.; Ni, W.; Herasimenka, Y.; Feruglio, L.; Montini, T.; Pérez-Juste, J.; Fornasiero, P.; Prato, M.; Liz-Marzán, L. M. Antibonding Plasmon Modes in Colloidal Gold Nanorod Clusters. *Langmuir* **2011**, ASAP.
33. Ahniyaz, A.; Sakamoto, Y.; Bergström, L. Magnetic Field-induced Assembly of Oriented Superlattices from Maghemite Nanocubes. *Proc. Natl. Acad. Sci. U. S. A.* **2007**, *104*, 17570–17574.
34. Huang, H.-T.; Zhang, B.-T.; He, J.-L.; Yang, J.-F.; Xu, J.-L.; Yang, X.-Q.; Zuo, C.-H.; Zhao, S. Diode-Pumped Passively Q-switched Nd:$Gd_{0.5}Y_{0.5}VO_4$ Laser at 1.34μm with V^{3+}:YAG as the Saturable Absorber. *Opt. Express* **2009**, *17*, 6946–6951.
35. Chen, J.; Lim, B.; Lee, E. P.; Xia, Y. Shape-Controlled Synthesis of Platinum Nanocrystals for Catalytic and Electrocatalytic Applications. *Nano Today* **2009**, *4*, 81–95.
36. Bishop, K. J. M.; Wilmer, C. E.; Soh, S.; Grzybowski, B. A. Nanoscale Forces and Their Uses in Self-Assembly. *Small* **2009**, *5*, 1600–1630.
37. Nie, Z.; Fava, D.; Kumacheva, E.; Zou, S.; Walker, G. C.; Rubinstein, M. Self-Assembly of Metal-Polymer Analogues of Amphiphilic Triblock Copolymers. *Nat. Mater.* **2007**, *6*, 609–614.
38. Korgel, B. A.; Fullam, S.; Connolly, S.; Fitzmaurice, D. Assembly and Self-Organization of Silver Nanocrystal Superlattices: Ordered "Soft Spheres". *J. Phys. Chem. B* **1998**, *102*, 8379–8388.
39. Grzelczak, M.; Vermant, J.; Furst, E. M.; Liz-Marzán, L. M. Directed Self-Assembly of Nanoparticles. *ACS Nano* **2010**, *4*, 3591–3605.
40. Bodnarchuk, M. I.; Kovalenko, M. V.; Heiss, W.; Talapin, D. V. Energetic and Entropic Contributions to Self-Assembly of Binary Nanocrystal Superlattices: Temperature as the Structure-Directing Factor. *J. Am. Chem. Soc.* **2010**, *132*, 11967–11977.
41. Min, Y.; Akbulut, M.; Kristiansen, K.; Golan, Y.; Israelachvili, J. The Role of Interparticle and External Forces in Nanoparticle Assembly. *Nat. Mater.* **2008**, *7*, 527–538.
42. Talapin, D. V.; Shevchenko, E. V.; Murray, C. B.; Titov, A. V.; Král, P. Dipole-Dipole Interactions in Nanoparticle Superlattices. *Nano Lett.* **2007**, *7*, 1213–1219.
43. Titov, A. V.; Král, P. Modeling the Self-Assembly of Colloidal Nanorod Superlattices. *Nano Lett.* **2008**, *8*, 3605–3612.
44. Clancy, P. Nanoparticles: Self-Assembly Finds Its Own Limits. *Nat. Nanotechnol.* **2011**, *6*, 540–541.
45. Henry, A.-I.; Courty, A.; Pileni, M.-P.; Albouy, P.-A.; Israelachvili, J. Tuning of Solid Phase in Supracrystals Made of Silver Nanocrystals. *Nano Lett.* **2008**, *8*, 2000–2005.
46. He, J.; Lin, X.-M.; Chan, H.; Vuković, L.; Král, P.; Jaeger, H. M. Diffusion and Filtration Properties of Self-Assembled Gold Nanocrystal Membranes. *Nano Lett.* **2011**, *11*, 2430–2435.
47. Chan, H.; Král, P. Self-standing Nanoparticle Membranes and Capsules. *Nanoscale* **2011**, *3*, 1881–1886.
48. Shevchenko, E. V.; Talapin, D. V.; Kotov, N. A.; O'Brien, S.; Murray, C. B. Structural Diversity in Binary Nanoparticle Superlattices. *Nature* **2006**, *439*, 55–59.
49. Ohara, P. C.; Leff, D. V.; Heath, J. R.; Gelbart, W. M. Crystallization of Opals from Polydisperse Nanoparticles. *Phys. Rev. Lett.* **1995**, *75*, 3466–3469.
50. Chen, Z.; Moore, J.; Radtke, G.; Sirringhaus, H.; O'Brien, S. Binary Nanoparticle Superlattices in the Semiconductor-Semiconductor System: CdTe and CdSe. *J. Am. Chem. Soc.* **2007**, *129*, 15702–15709.
51. Yamamuro, S.; Sumiyama, K.; Kamiyama, T. Shape-Induced Simple Cubic Arrangement in Three-Dimensional Nanocube Self-Assemblies. *Appl. Phys. Lett.* **2008**, *92*, 113108.
52. Stoeva, S. I.; Prasad, B. L. V.; Uma, S.; Stoimenov, P. K.; Zaikovski, V.; Sorensen, C. M.; Klabunde, K. J. Face-Centered Cubic and Hexagonal Closed-Packed Nanocrystal Superlattices of Gold Nanoparticles Prepared by Different Methods. *J. Phys. Chem. B* **2003**, *107*, 7441–7448.
53. Stebe, K. J.; Lewandowski, E.; Ghosh, M. Oriented Assembly of Metamaterials. *Science* **2009**, *325*, 159–160.
54. Henzie, J.; Grünwald, M.; Widmer-Cooper, A.; Geissler, P. L.; Yang, P. Self-Assembly of Uniform Polyhedral Silver Nanocrystals into Densest Packings and Exotic Superlattices. *Nat. Mater.* **2011**, 10.1038/NMAT3178.
55. Motte, L.; Billoudet, F.; Lacaze, E.; Douin, J.; Pileni, M. P. Self-Organization into 2D and 3D Superlattices of Nanosized Particles Differing by Their Size. *J. Phys. Chem. B* **1997**, *101*, 138–144.
56. Demortiére, A.; Petit, C. First Synthesis by Liquid-Liquid Phase Transfer of Magnetic Co_xPt_{100-x} Nanoalloys. *Langmuir* **2007**, *23*, 8575–8584.
57. Kraig, R. E.; Roundy, D.; Cohen, M. L. A Study of the Mechanical and Structural Properties of Polonium. *Solid State Commun.* **2004**, *129*, 411–413.
58. Li, F.; Delo, S. A.; Stein, A. Disassembly and Self-Reassembly in Periodic Nanostructures: A Face-Centered-to-Simple-Cubic Transformation. *Angew. Chem., Int. Ed.* **2007**, *46*, 6666–6669.
59. Yamamuro, S.; Sumiyama, K. Why Do Cubic Nanoparticles Favor a Square Array? Mechanism of Shape-Dependent Arrangement in Nanocube Self-Assemblies. *Chem. Phys. Lett.* **2006**, *418*, 166–169.
60. Yao, H.; Minami, T.; Hori, A.; Koma, M.; Kimura, K. Fivefold Symmetry in Superlattices of Monolayer-Protected Gold Nanoparticles. *J. Phys. Chem. B* **2006**, *110*, 14040–14045.
61. Cölfen, H.; Mann, S. Higher-Order Organization by Mesoscale Self-Assembly and Transformation of Hybrid Nanostructures. *Angew. Chem., Int. Ed.* **2003**, *42*, 2350–2365.
62. Novell-Leruth, G.; Valcárcel, A.; Clotet, A.; Ricart, J. M.; Pérez-Ramírez, J. DFT Characterization of Adsorbed NH_x Species on Pt(100) and Pt(111) Surfaces. *J. Phys. Chem. B* **2005**, *109*, 18061–18069.
63. Hamaker, H. C. The London - Van der Waals Attraction between Spherical Particles. *Physica* **1937**, *4*, 1058–1072.
64. Luedtke, W. D.; Landman, U. Structure, Dynamics, and Thermodynamics of Passivated Gold Nanocrystallites and Their Assemblies. *J. Phys. Chem.* **1996**, *100*, 13323–13329.
65. MacKerell, A. D.; Bashford, D.; Bellott, M.; Dunbrack, R. L.; Evanseck, J. D.; Field, M. J.; Fischer, S.; Gao, J.; Guo, H.;

Ha, S.; *et al*. All-Atom Empirical Potential for Molecular Modeling and Dynamics Studies of Proteins. *J. Phys. Chem. B* **1998**, *102*, 3586–3616.
66. Ionita, P.; Volkov, A.; Jeschke, G.; Chechik, V. Lateral Diffusion of Thiol Ligands on the Surface of Au Nanoparticles: An Electron Paramagnetic Resonance Study. *Anal. Chem.* **2007**, *80*, 95–106.
67. Schapotschnikow, P.; Pool, R.; Vlugt, T. J. H. Molecular Simulations of Interacting Nanocrystals. *Nano Lett.* **2008**, *8*, 2930–2934.
68. Phillips, J. C.; Braun, R.; Wang, W.; Gumbart, J.; Tajkhorshid, E.; Villa, E.; Chipot, C.; Skeel, R. D.; Kalé, L.; Schulten, K. Scalable Molecular Dynamics with NAMD. *J. Comput. Chem.* **2005**, *26*, 1781–1802.
69. Humphrey, W.; Dalke, A.; Schulten, K. VMD: Visual Molecular Dynamics. *J. Mol. Graphics* **1996**, *14*, 33–38.
70. Darden, T.; York, D.; Pedersen, L. Particle Mesh Eward: An N**log*(N) Method for Ewald Sums in Large Systems. *J. Chem. Phys.* **1993**, *98*, 185503.